



## Neural Networks in Optimizing the Performance of the Elliptical-Plasmonic Sensor

Khaikal Ramadhan <sup>1\*</sup>, Andi M. N. F. Syamsul <sup>1</sup>, Arip Marwan <sup>2</sup>, Beny Agustirandi <sup>1</sup>, Mhd Yasir <sup>1</sup>, Hadi Christian <sup>3</sup>

<sup>1</sup> Department of Physics, Faculty of Mathematics and Natural Science, Institut Teknologi Bandung, Bandung 40132, Indonesia.

<sup>2</sup> Department of Electrical Engineering, Faculty of Engineering, University of Riau, Pekanbaru, 28293, Indonesia.

<sup>3</sup> Department of Engineering Physics, Faculty of Engineering, Institut Teknologi Bandung, Bandung 40116, Indonesia.

### Abstract

In this work, we report the capability of a PCF-SPR sensor with an elliptical core, which has high sensitivity, and it is explained using a machine learning approach. The sensor component consists of fused silica as the background material, TiO<sub>2</sub> as the adhesive material between the dielectric material and the plasmonic material, and Au was chosen as plasmonic material with optimal thicknesses of 35 nm for TiO<sub>2</sub> and 45 nm for Au. Numerical results show that the sensor component has a high sensitivity of 24,000 nm/RIU for four modes that have consistent shifts, including x-polarized, x-odd, y-polarized, and y-odd. Meanwhile, AS maximums were found of -91.82 1/RIU for x-polarized, -91.88 1/RIU for y-polarized, -90.98 1/RIU for x-odd, and -89.276 1/RIU for y-odd respectively, on the refractive index of the analyte of 1,365 RIU. The ML algorithm was used to optimize the sensor parameters, and it was found that the algorithm had a very low MSE of 0.00083; this result is better than the previous report work.

### Keywords:

Elliptical-Photonic Crystal Fiber; Machine Learning; Optical Sensor; Surface Plasmon Resonance.

### Article History:

Received:	27	February	2024
Revised:	02	August	2024
Accepted:	11	August	2024
Published:	01	October	2024

## 1- Introduction

The surface plasmon resonance sensor is a component that works through the process of electron oscillation between the metal plate and the dielectric layer. This event is interesting because the wavelength of the pump light has a direction parallel to the wavelength of the surface electrons. This phenomenon is the trigger for the very rapid development of sensor components SPR-based [1]. Some of the properties possessed by model components like this are very high sensitivity, good accuracy, detection in a wide range with high resolution, very fast response time, label-free, and a small size [2–5]. Some optical-based sensor components are classically large and inefficient, such as fiber Bragg grating sensors [6, 7], optical fiber [8, 9], SPR based on prism [10], and waveguide [11]. Therefore, it cannot meet the needs of sensors that are portable, low-cost, and tend to be small. To overcome this deficiency, a photonic crystal fiber sensor based on surface plasmon resonance (PCF-SPR) provides high sensitivity [12], remote sensing capabilities, portability of sensor size, fast response, and ultra-low loss [2, 13, 14]. PCF-SPR has air holes around the core, making it possible to manipulate light, and also has a metal layer both inside the air holes and on the outer layer [15]. Until now, the development of this sensor component has been very rapid; various types of geometric structures have been reported, some of which have good performance, such as D-shaped PCF-SPR [16], PCF-SPR, which has multi-analyte and multi-

\* CONTACT: [khaikalramadhan37@gmail.com](mailto:khaikalramadhan37@gmail.com)

DOI: <http://dx.doi.org/10.28991/ESJ-2024-08-05-07>

© 2024 by the authors. Licensee ESJ, Italy. This is an open access article under the terms and conditions of the Creative Commons Attribution (CC-BY) license (<https://creativecommons.org/licenses/by/4.0/>).

channel capabilities [17, 18], PCF-SPR with unique air holes, etc. [19]. So, the manipulation of the geometric structure of PCF-SPR shows unique capabilities.

The PCF-SPR sensor component has recently been reported to have good capabilities in various applications, including in the medical world, where the highly sensitive PCF-SPR can detect very small refractive index changes in various disease-infected substances and normal substances, such as PCF-SPR can detect changes in the refractive index in cells infected with breast cancer, cells infected with skin cancer, cells infected with blood cancer, cells infected with tuberculosis, and various types of cells infected with other diseases. Ramola et al. (2021) proposed a PCF-SPR sensor design for detecting various types of cancer cells with an external sensing scheme where the analyte is placed on the outer layer of the sensor. The sensor is composed of fused silica material as the background sensor material, gold as the SPR material, and a TiO<sub>2</sub> layer as the adhesive. In the design, it is found that the sensor has a maximum wavelength sensitivity of 14285.71 nm/RIU and 12857.14 nm/RIU for TE and TM, respectively, while the sensor resolution is  $7.77 \times 10^{-6}$  and  $7 \times 10^{-6}$ , respectively, for TM and TE. The types of cancer cells that can be detected are skin, blood, cervical, adrenal gland, breast cancer type 1 and type 2 [20].

Hoseinian et al. (2021) reported a PCF SPR sensor with a very unique geometric structure for detecting cancer cells. In their design, the sensor sensitivity was obtained at 62,000 nm/RIU, 84,000 nm/RIU, and 135,000 nm/RIU for each CL peak, peak 1, peak 2, and peak 3 [21]. Kumar et al. (2023) reported that the PCF-SPR sensor can detect various types of cancer cells with the help of Machine Learning to optimize sensor performance. The sensor has a unique geometric structure composed of silica, MXENE, and gold materials, with a thickness of the gold and MXENE layers each of 40 nm. and 14 nm. In the design, the maximum WS is obtained at 10,714 nm/RIU (x-polarized) and 13,071 nm/RIU (y-polarized) for the MCF-7 cell [22]. Singh & Prajapati (2023) reported a side-polished PCF plasmonic sensor for detecting dangerous cancer cells. The proposed sensor is D-shaped with an external sensing scheme, and the sensor is composed of silica, TiO<sub>2</sub>, and gold materials. The sensor is reported to be able to detect various types of cancer cells, including cervical cancer, blood cancer, skin cancer, adrenal gland cancer, breast cancer 1, and breast cancer 2. The maximum WS was obtained for each hela, Jurkat, basal, PC12, and MDA-MB cancer cell. -231 and MCF-7 are 20,000 nm/RIU, 22,857 nm/RIU, 20,000 nm/RIU, 20,714 nm/RIU, 21,428 nm/RIU, and 25,000 nm/RIU [23]. Recently, Ehyae et al. (2023) also reported dual-core PCF in detecting cancer cells. The PCF was built using silica material with an internal sensing scheme. The proposed sensor has a max ws of 12,500 nm/RIU and a max FOM of 22.03 1/RIU for basal cells [24]. Mittal et al. (2023) reported the spiral-shaped PCF-SPR component in detecting cancer cells. The component was composed of silica and gold materials. In the design, it was found that the sensor had a detection range from 1.36 to 1,401 RIU, and the component had an amplitude sensitivity and sensor resolution of 289, respectively. 1/RIU and  $2.33 \times 10^{-4}$  [25].

In PCF-SPR, the geometry determines the effective refractive index distribution of the sensor; various types of elliptical air holes around the core have been reported. Yan et al. (2021) reported a PCF-SPR sensor component with one of the elliptical air holes; a layer of gold also covers the air holes. This ellipse has a thickness of 40 nm; meanwhile, the side ratio of the air holes of this ellipse is 0.7; this component has a narrow detection range of 1.43 - 1.49 RIU; meanwhile, the maximum WS is 12,719.97 nm/RIU; meanwhile, AS is not counted in the research [26]. Otupiri et al. (2015) reported multi-channel PCF-SPR with an elliptical air hole with a gold thickness of 45 nm. The sensor component has a maximum WS of 4600 nm/RIU, with a detection range of 1.32 to 1.36 RIU for channels 2 and 1.33 for channel 1 [27]. Li et al. (2023) also reported good capabilities of the D-shaped PCF-SPR sensor component with one elliptical air hole. The sensor component has a WS of 19,600 nm/RIU with a detection range of 1.37 to 1.42 nm/RIU, while the AS is 2300 1/RIU, and one of the elliptical air holes has a dimensional ratio of 0.333 [28]. However, the capabilities of PCF-SPR can still be improved by using Machine Learning to predict the optimal size of the sensor geometry.

Machine Learning (ML) is a method for learning and testing information from large data; of course, it can also be applied in optical sensing analysis. Several popular packages are usually used in ML platforms, such as TensorFlow, Keras, Scikit Learn, and Keras, which are used for developing, training, and validating neural networks. Several researchers have reported their work using machine learning in predicting and analyzing data from optical sensors. Kumar et al. (2023) reported PCF-SPR components in detecting cancer cells. In their work, ML was implemented to optimize structural parameters and predict the refractive index of the core mode and core loss and obtained a low mean squared error of 0.01525 [22]. Kalyoncu et al. (2022) used machine learning to estimate the bent properties of PCPR. KNNR is recommended for estimating loss in PCF-SPR components, and it is believed that KNNR does not require a long training process [29]. In other work, Li et al. (2023) used a support vector machine based on radial basis functions to predict optical materials in photonic crystal fibers; some of the parameters predicted were effective refractive index, chromatic dispersion, and confinement loss [30]. Recently, Kumar et al. (2023) also used ML to analyze the performance of the PCF-SPR sensor in detecting malaria based on RBCs and obtained an MSE of 0.01526 [31]. Dogan et al. (2023) used artificial neural networks to optimize Ag on D-shaped optical components in detecting refractive index. 119 input data were used as training data from FEM simulation results and obtained a predicted wavelength sensitivity of 3890 nm/RIU when the air gap distance between gratings was 10 nm, gratings 20, residual cladding thickness 50 nm, and silver thickness 75 nm [32].

In this paper, we optimize a machine learning algorithm to predict the optical parameters of a surface plasmon resonance-based photonic crystal fiber sensor component with a single elliptical air hole. The machine learning model includes more input parameters than previously reported, and the algorithm demonstrates a very low error rate of 0.00083. Additionally, optimization has been performed on the sensor's geometric structure, resulting in an algorithm suitable for analyzing sensor performance with high sensitivity. Finite element analysis results indicate that the sensor component achieves a maximum wavelength sensitivity (WAS) of 24,000 nm/RIU, which exceeds previously reported values. Meanwhile, the maximum ultra-sensitivity (US) values reached -91.82 1/RIU for x-polarization, -91.88 1/RIU for y-polarization, -90.98 1/RIU for x-odd mode, and -89.276 1/RIU for y-odd mode, at a refractive index of 1.365 RIU.

## 2- Geometry of Sensor

The industry has a strong demand for geometric structures with high performance. The geometric structure of the PCF-SPR sensor in this study is shown in Figure 1. The sensor is designed using the finite element full-vector method (FVFEM) in COMSOL Multiphysics. To restrict energy loss on unwanted surfaces, the design includes a perfectly matched layer (PML) with a thickness of 1  $\mu\text{m}$ , which confines energy within the PCF surface, concentrating it on the PCF core. The 2D design comprises a mesh grid over the sensor, allowing Maxwell's equations to be represented by a matrix of eigenvalues, yielding both real and imaginary representations of the core mode. The diameters of the air holes around the sensor core are defined as  $d_1 = 0.49 \mu\text{m}$ ,  $d_2 = 0.592 \mu\text{m}$ , and  $d_3 = 0.74 \mu\text{m}$ . A unique arrangement of air holes in the sensor's cross-section enhances performance, with an elliptical air hole at the center of the PCF core, sized at  $a = 0.49 \mu\text{m}$  and  $b = 0.37 \mu\text{m}$ . Fused silica is used as the background material and is defined using the Sellmeier equation. This silica is coated with a 35 nm layer of  $\text{TiO}_2$  as an adhesive, followed by a 45 nm layer of plasmonic gold, chosen for its superior chemical stability compared to other materials. The analyte layer has a chamber width of 50 nm. Fused silica material properties are further defined in Equation 1, with each symbol's value detailed in Table 1 [33].

$$n(\lambda) = \sqrt{1 + \frac{A_1\lambda^2}{\lambda^2 - B_1} + \frac{A_2\lambda^2}{\lambda^2 - B_2} + \frac{A_3\lambda^2}{\lambda^2 - B_3}} \quad (1)$$

Here,  $n$  represents the refractive index (RI) of  $\text{SiO}_2$ , which varies with the wavelength  $\lambda$ . The values for each variable are listed in Table 1. The properties of the gold material are defined using the Drude-Lorentz model, as expressed in Equation 8, with variable values provided in Table 2. The permittivity of Au is calculated using the Drude-Lorentz model, shown in Equation 2, with corresponding variable values detailed in Table 2.

$$\epsilon_{au} = \epsilon_\infty - \frac{\omega_D^2}{\omega(\omega + j\gamma_D)} - \frac{\Delta\epsilon\Omega_L^2}{(\omega^2 - \Omega_L^2) + j\Gamma_L\omega} \quad (2)$$

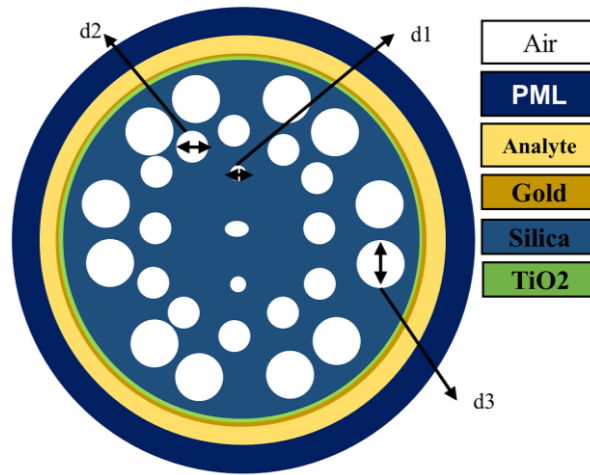


**Figure 1.** Sensor geometry structure with air hole geometry along the core with diameter  $d_1 = 0.49 \mu\text{m}$ ,  $d_2 = 0.592 \mu\text{m}$ , and  $d_3 = 0.74 \mu\text{m}$

**Table 1.** Value of Sellmeier equation [33]

Symbols	Value
A1	0.696163
A2	0.4079426
A3	0.897479400
B1	0.0046791486
B2	0.0135120631
B3	97.9340025

**Table 2. Value of the Drude-Lorentz equation [34]**

Symbols	Definition	Value
$\epsilon_{Au}$	Permittivity Value of Gold	5.9673
$\omega$	plasma frequency	$2\pi/0.75 \mu\text{m}$
$\gamma_D$	damping frequency	31.84 $\pi$ THz
$\omega_D$	plasmon frequency	4227.2 $\pi$ THz
$\Omega_L$	Oscillator Power	1300.14 $\pi$ THz
$\Gamma_L$	Spectral width	209.72 $\pi$ THz

### 3- Results and Discussion

The electromagnetic field that penetrates the sensor surface is transmitted through the PCF. Figures 2-a and 2-b show the electric field distribution on the sensor surface polarized along the x-axis, while Figures 2-c and 2-d show polarization along the y-axis. In this example, the analyte refractive index is 1.36 RIU, with a center wavelength of 1550 nm, the gold thickness of 40 nm, and TiO<sub>2</sub> thickness of 40 nm. The finite element method (FEM) is used to solve Maxwell's equations and determine the effective refractive index eigenvalues across the sensor's cross-section. This effective refractive index is a complex function, where its real part defines the surface modes of the sensor (core mode, cladding mode, and SPP mode). The imaginary part of the effective refractive index indicates signal loss, which can be calculated using Equation 3. The PML layer, located on the outermost layer of the sensor cross-section, absorbs light into the PCF.

$$L_c(\text{dB/cm}) = \left(\frac{4\pi f}{c}\right) \text{Im}(n_{\text{eff}}) \times 10^4 \quad (3)$$

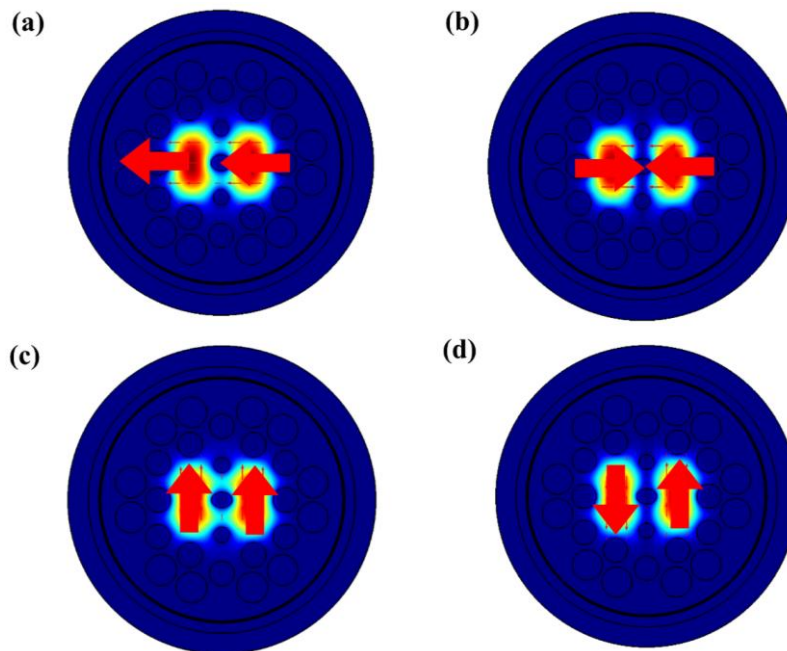


**Figure 2. Transverse Electric distribution in the cross-section of fiber components with differences in polarization around the cross-section of (a) polarization on the x-axis for both cores, (b) polarization on the x-odd axis, (c) polarization on the y-axis for both cores and (d) polarization on y-up and y-down for each core.**

Surface plasmon resonance in photonic crystal fiber (PCF) components occurs at the interface between the dielectric material and the metal layer. When light is polarized and decays within the cladding and metal layers, it forms an evanescent wave that propagates along the analyte and metal layers, resulting in surface plasmon excitation on the metal surface. These waves are highly sensitive to changes in the analyte's refractive index. The polariton plasmon wave vector can be determined using Equation 4.

$$K_{sp} = \frac{\omega}{c} \sqrt{\frac{\epsilon_{Au}\epsilon_{Analyte}}{\epsilon_{Au} + \epsilon_{Analyte}}} \quad (4)$$

Here,  $K_{sp}$  is the surface plasmon polariton (SPP) wave vector, which represents the frequency of the incident light,  $c$  is the speed of light in a vacuum, and the permittivities correspond to the gold and analyte, respectively. The vector components of evanescent waves propagating along the fiber and metal surfaces can be determined using Equation 5. When the SPP wave vector equals the evanescent wave vector, the SPR phenomenon occurs, as described by Equations 4 and 5.

$$K_{sp} = \frac{\omega}{c} \sqrt{\epsilon_{Fiber}} \sin\theta \quad (5)$$

### 3-1-Thickening the Thickness of a Thin Layer of Gold Against Confinement Loss

When exposed to electromagnetic waves, thin plasmonic materials cause electrons on their surface to oscillate, creating surface plasmon resonance (SPR). Various plasmonic materials, such as gold, silver, and aluminium, are used in SPR sensors. In this study, a gold coating is employed because gold is chemically more stable than other plasmonic materials and offers high sensitivity. This was confirmed by research conducted by Deepak Kumar, who evaluated the performance of PCF-SPR sensors with different plasmonic materials. He found a sensitivity of 1830.76 nm/RIU for gold, 1799 nm/RIU for silver, 1732 nm/RIU for aluminium, 1652 nm/RIU for copper, and 1532.2 nm/RIU for a gold-tin alloy [35]. The choice of plasmonic material significantly affects sensor performance. Gold, which is more chemically stable than silver (which is prone to oxidation and can reduce sensor accuracy), was chosen for this work [36]. Gold thickness was varied from 30 to 50 nm in 5 nm increments.

Figure 3 shows the peak shift of confinement loss for each gold thickness variation, with the analyte refractive index and  $\text{TiO}_2$  thickness kept constant at 1.36 RIU and 35 nm, respectively. The results indicate that thicker gold layers result in smaller confinement losses, as light struggles to penetrate thicker layers. Among polarizations, y-odd polarization shows the highest confinement loss, while x-axis polarization has the lowest. Resonance wavelength peaks for each gold thickness are observed at 660 nm, 680 nm, 690 nm, and 700 nm for thicknesses of 30 nm, 35 nm, 40 nm, 45 nm, and 50 nm, respectively. These results align with findings reported by Sakib et al., who also observed resonance peak shifts to higher wavelengths with increasing gold thickness [3], as well as Majeed et al., who found that increasing gold thickness causes resonance peaks to decrease and shift to higher wavelengths [37].

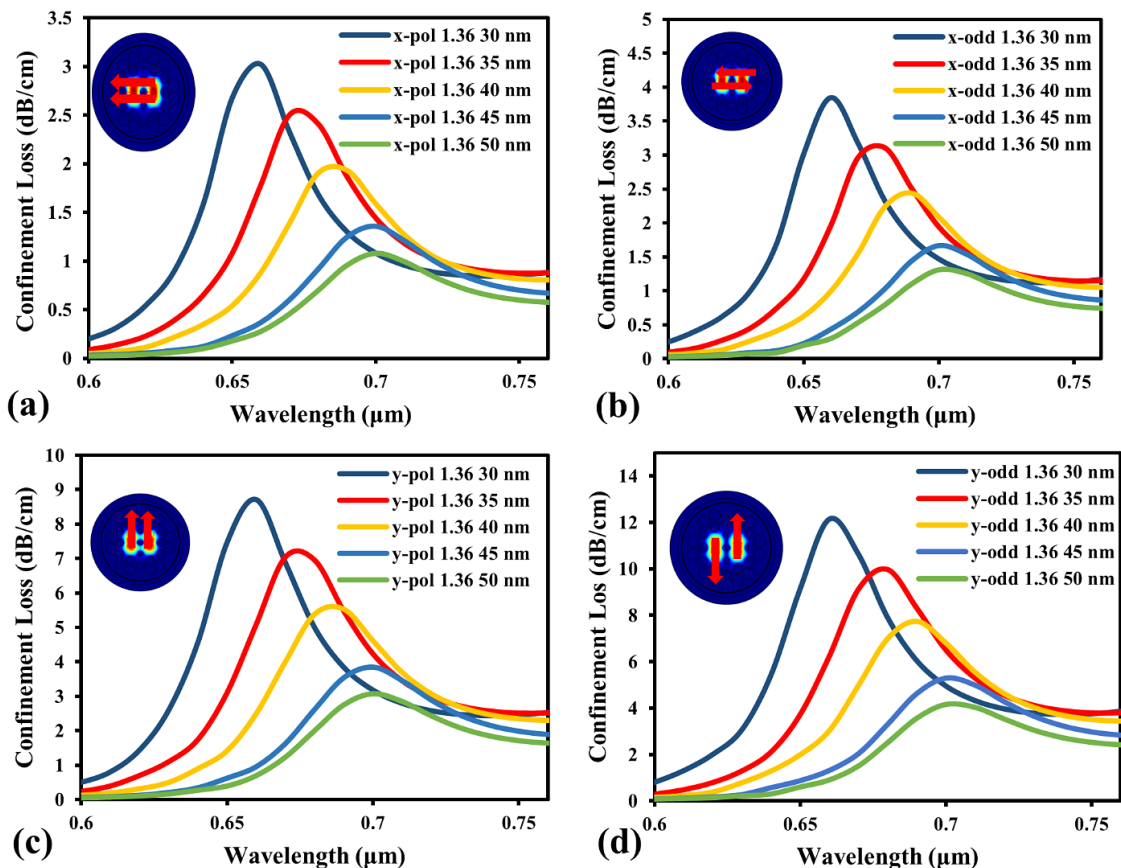


**Figure 3.** Variation of confinement loss (imaginer effective refractive index of dual-core sensor cross-section) for each thickness of gold with variations from 30 nm (blue lines), 35nm (red lines), 40 nm (yellow lines), 45 nm (light blue lines), and 50 nm (soft green lines), analyte refractive index set constant 1.36 RIU and thickness  $\text{TiO}_2 = 35$  nm, (a) polarization on the x-axis for both cores, (b) polarization in the x-odd cross-section of the sensor, (c) polarization in y-pol, and (d) polarization in y-odd.

### 3-2-Effect of the Thin Layer Thickness of $\text{TiO}_2$ on Confinement Loss

Non-toxic adhesives and inorganic materials like  $\text{TiO}_2$  do not significantly alter peak resonance wavelengths, making them ideal as dielectric coatings with plasmonic materials. Figure 4 illustrates the effect of varying  $\text{TiO}_2$  thickness from

30 to 50 nm while keeping the gold layer constant at 45 nm. A thinner  $\text{TiO}_2$  layer results in high confinement loss in the component due to the deep penetration of the core mode into the SPP mode. As  $\text{TiO}_2$  thickness increases, the peak confinement loss weakens, reaching a minimum value across all polarization modes—x-polarized, y-polarized, x-odd, and y-odd—following the same trend. This confinement loss is considerably lower than reported in previous studies [5, 38, 39]. Regardless of  $\text{TiO}_2$  thickness, the peak confinement loss remains constant at a resonance wavelength of 700 nm across all core modes, indicating that the plasmonic material does not reduce wavelength sensitivity in the sensor components.

Other studies support these findings, showing that variations in  $\text{TiO}_2$  layer thickness have little impact on confinement loss, as reported by Ibrahim et al. [40] in PCF-SPR sensors coated with graphene, Au, and  $\text{TiO}_2$  for cancer cell detection. However, some studies have shown significant effects of  $\text{TiO}_2$  thickness variations with different PCF-SPR designs [13, 41, 42].

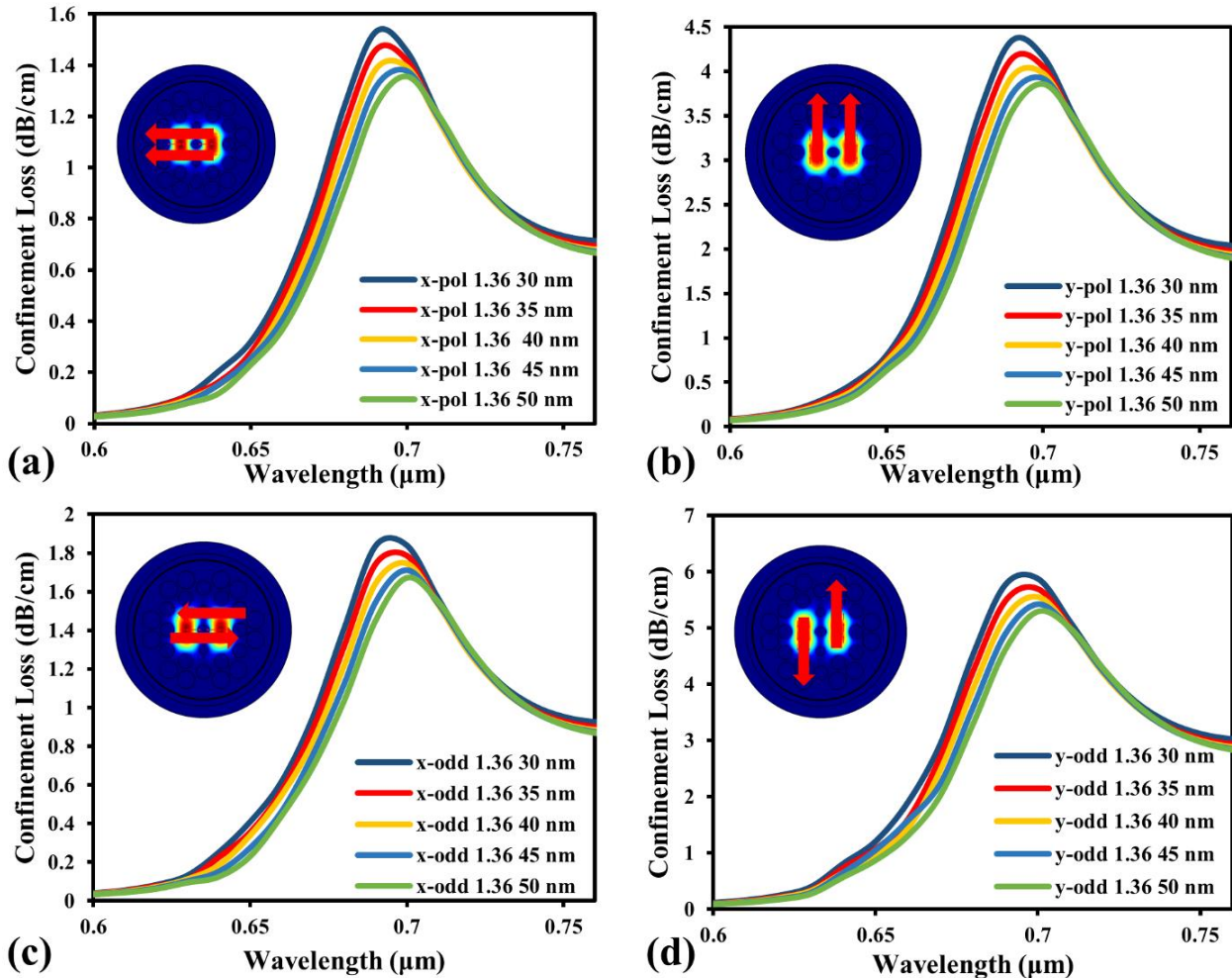


**Figure 4.** Variation of confinement loss (imaginer effective refractive index of sensor cross-section) for each thickness of  $\text{TiO}_2$  with variations of 30 nm, 35 nm, 40 nm, 45 nm, and 50 nm, analyte refractive index set constant 1.36 RIU (a) polarization on the x-axis for both cores, (b) polarization on the x-odd cross-section of the sensor, (c) polarization on y-pol, and (d) polarization on y-odd.

### 3-3-Effect of Air Hole Diameter on Confinement Loss

In this section, variations in the air hole diameter around the sensor cross-section are examined, with sizes ranging from 1.48 to 1.52 μm, as shown in Figure 5. The effect of air hole diameter variations on the sensor's peak confinement loss was analyzed with an analyte refractive index of 1.36 RIU. The simulation results show that changes in resonance wavelength are minimal, with each air hole diameter producing the same resonance wavelength at 690 nm. This trend is consistent across all core modes of the sensor. Notably, low confinement loss remains stable across variations in air hole diameter. Maximum loss occurs in the Y-odd and Y-polarized core modes, while minimal loss is observed in the X-polarized and X-odd core modes. Sarker's research confirms that peak resonance remains unchanged despite variations in the diameter of the air holes [41]. Islam also reports that loss trends are higher for smaller diameters and decrease with larger diameters [43].

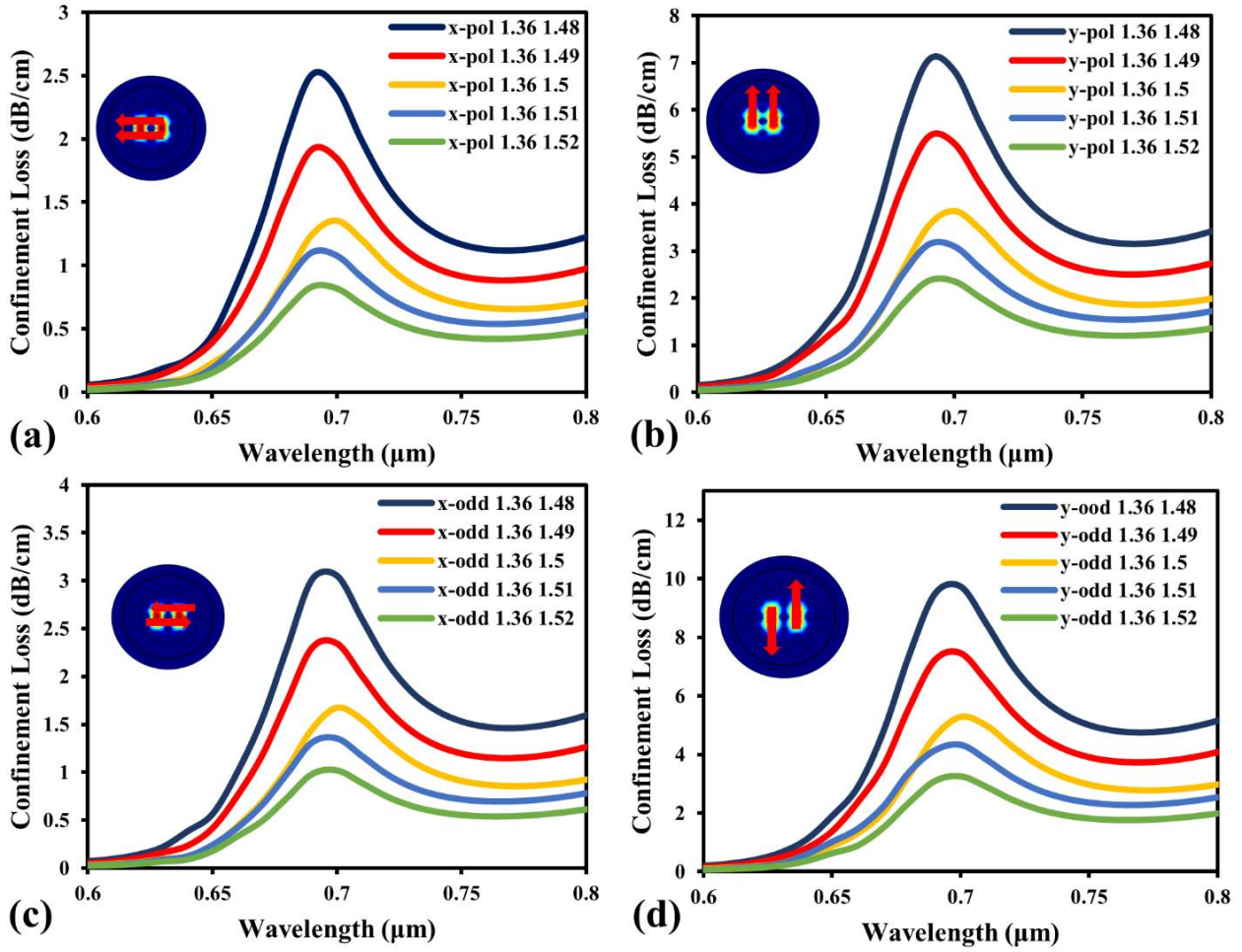


**Figure 5.** Variation in the diameter of the air hole around the sensor cross-section against confinement loss, with gold thickness 45 nm, thickness  $\text{TiO}_2 = 35$  nm, refractive index of analyte 1.36 RIU, diameter size 1.48  $\mu\text{m}$  (blue line), 1.49  $\mu\text{m}$  (red line), 1.5  $\mu\text{m}$  (yellow line), 1.51  $\mu\text{m}$  (blue light line) and 1.52  $\mu\text{m}$  (green light line), (a) polarization on the x-axis of the sensor cross-section, (b) polarization on the x-odd, (c) polarization on the c-axis, and (d) polarization on y-odd.

### 3-4- Resonance Wavelength Analysis

Resonance wavelength is a critical benchmark for evaluating the performance of PCF-SPR-based sensors. It refers to the wavelength that produces the highest peak value of confinement loss. A significant shift in resonance wavelength in response to slight changes in the refractive index indicates enhanced sensitivity of the optical sensor. Figure 6 illustrates the trend of resonance wavelength shifts for various changes in refractive index. This shift trend is plotted for each core mode: Figure 6-a for x-polarized, Figure 6-b for x-odd, Figure 6-c for y-polarized, and Figure 6-d for y-odd. In this case, the thicknesses of gold and  $\text{TiO}_2$  are set at 50 nm and 35 nm, respectively. The sensor can detect analyte refractive index values in the range of 1.34 to 1.38 RIU, with increments of 0.5 RIU.

As the analyte refractive index increases across all core mode trends, peak confinement loss also rises. Although this simulation shows very low loss values compared to previous studies, this low loss is advantageous for the sensor's measurement accuracy. The resonance wavelength shifts for each refractive index range show promising results, with sensitivity increasing as the analyte refractive index grows. For the range of 1.335 to 1.34 RIU, the wavelength sensitivity (WS) is 2000 nm/RIU, while the highest WS is observed in the range from 1.375 to 1.38 RIU, reaching 24,000 nm/RIU. These results indicate strong performance compared to previous studies. This study emphasizes the use of machine learning to predict and analyze data from FEM simulation results. WS is calculated using Equation 6, where  $\Delta n_a$  represents the change in analyte refractive index, and  $\Delta \lambda_{peak}$  is the peak shift in confinement loss between two analyte refractive indices.

$$S_\lambda(\text{nm/RIU}) = \frac{\Delta \lambda_{peak}}{\Delta n_a} \quad (6)$$

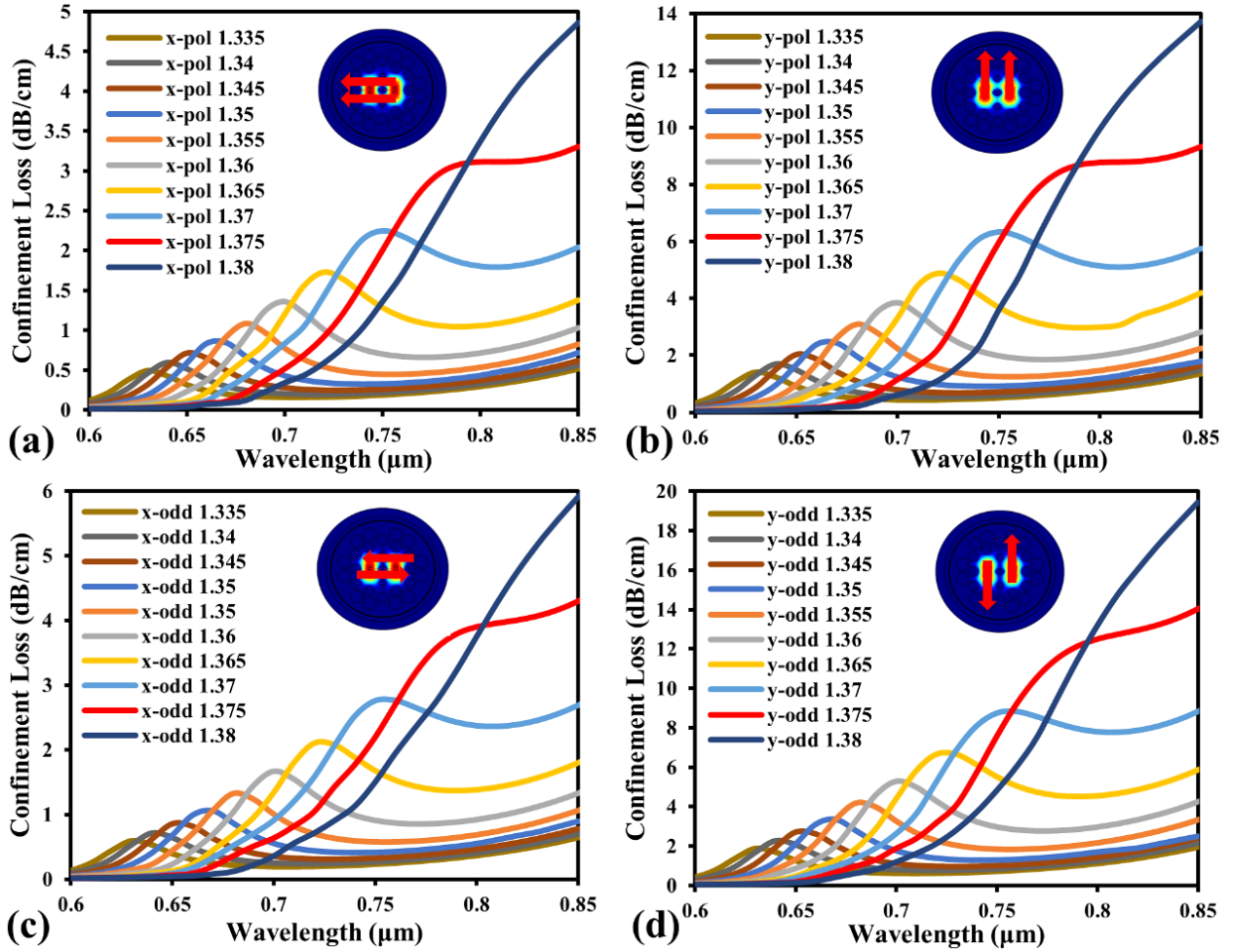


**Figure 6.** component confinement loss distribution for each analyte refractive index of 1.34, 1.345, 1.35, 1.355, 1.36, 1.365, 1.37, 1.375, 1.38 RIU at each polarization of the sensor cross-section, the thickness of gold and TiO<sub>2</sub> is set constant with the respective values of  $t_{\text{TiO}_2} = 35$  nm, and  $t_g = 50$ nm, (a) polarization on the x-axis, (b) polarization on x-odd, (c) polarization on y, and (d) polarization at y-odd.

Meanwhile, the figure of merit (FOM) is a crucial parameter for assessing the performance of a sensor. FOM can be mathematically defined by the equation below. It represents the ratio of the device's sensitivity to half the width of the resonant peak height (FWHM). In SPR sensor design, the FOM is typically less than 100 [44]. In this component, the FOM achieved is 18 1/RIU for a refractive index of 1.335 RIU, with an FWHM of 20 nm.

### 3-5-Amplitude Sensitivity Analysis

Amplitude sensitivity is another parameter used to measure sensor performance. It is determined by the difference between two confinement losses in the nearest refractive index range. Figure 7 illustrates the amplitude sensitivity for detecting analyte refractive indices ranging from 1.34 RIU to 1.38 RIU. Each core mode shows a similar trend in peak shifts, although the peak confinement loss values differ. The peaks for each analyte refractive index are as follows: 1.34 RIU has a peak at 650 nm, 1.345 RIU at 660 nm, 1.35 RIU at 680 nm, 1.355 RIU at 690 nm, 1.36 RIU at 710 nm, 1.365 RIU at 740 nm, 1.37 RIU at 770 nm, and 1.375 RIU at 810 nm. The shifts in peak values exhibit an increasing trend with rising analyte refractive indices. Amplitude sensitivity (AS) is calculated using Equation 7, where  $\partial\alpha(\lambda, n_a)$  represents the change in confinement loss for two adjacent analyte refractive indices. In this sensor component, the maximum amplitude sensitivity values were found to be -91.82 1/RIU for x-polarized, -91.88 1/RIU for y-polarized, -90.98 1/RIU for x-odd, and -89.276 1/RIU for y-odd at a refractive index of 1.365 RIU, respectively.

$$S_A(1/RIU) = -\frac{1}{\alpha(\lambda, n_a)} \frac{\partial\alpha(\lambda, n_a)}{\partial n_a} \quad (7)$$

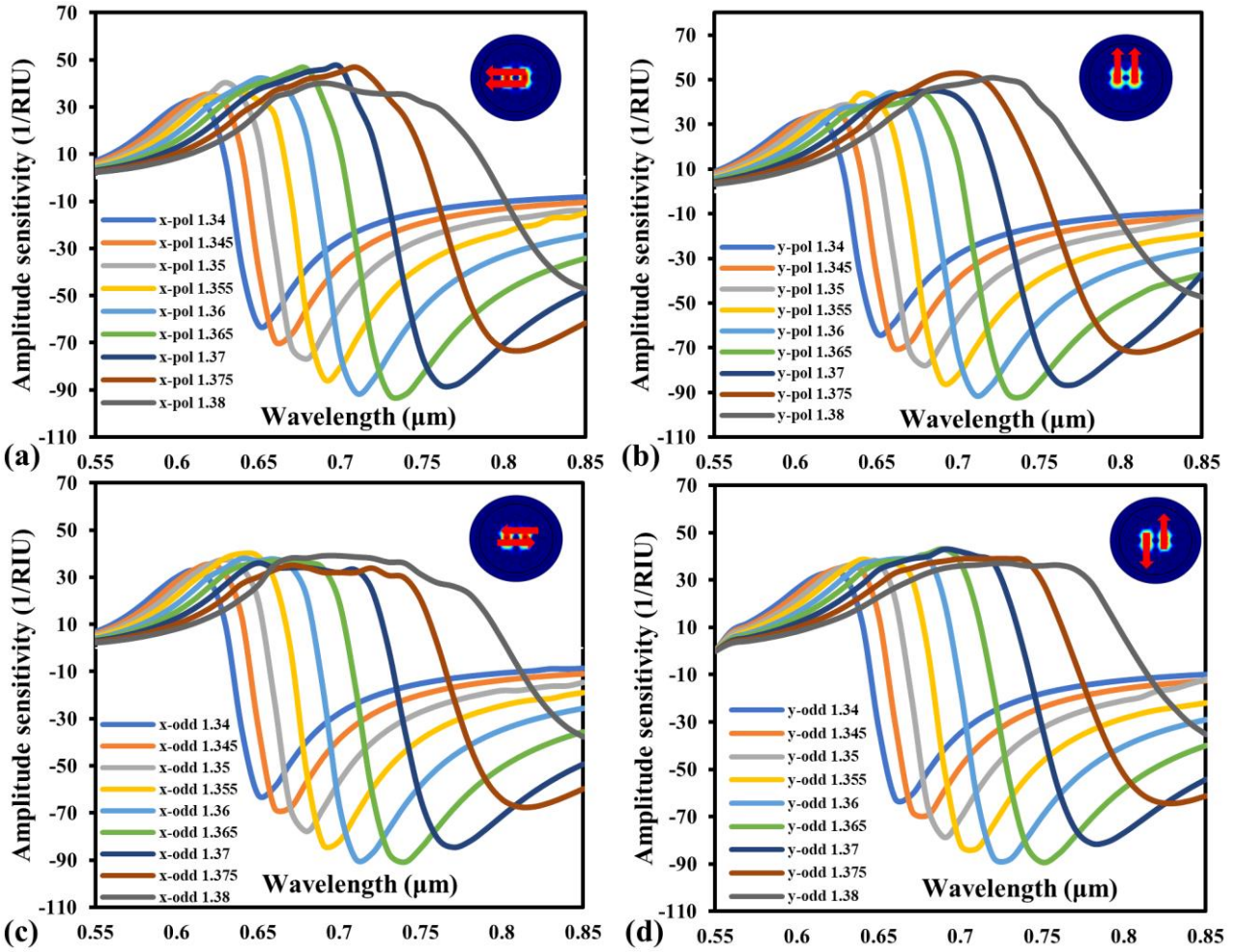


**Figure 7.** The component amplitude distribution for each analyte refractive index of 1.34, 1.345, 1.35, 1.355, 1.36, 1.365, 1.37, 1.375, 1.38 RIU at each polarization of the sensor cross-section, the thickness of gold and  $\text{TiO}_2$  is set constant with respective values of  $t_{\text{TiO}_2} = 35 \text{ nm}$ , and  $t_g = 50 \text{ nm}$ , (a) polarization on the x-axis, (b) polarization on x-odd, (c) polarization on y, and (d) polarization at y-odd.

### 3-6- Machine Learning Approach in Sensor Component

Sensors designed for optimal performance require precise geometric parameters. Achieving this precision can be done by utilizing machine learning (ML) algorithms to predict and optimize the geometric structure of sensors. Artificial Neural Networks (ANN) are a subset of ML techniques that excel in training models for predicting specific parameters within datasets. In this study, numerical results obtained through Finite Element Method (FEM) simulations serve as the basis for creating ML training datasets. The datasets encompass various parameters such as gold thickness,  $\text{TiO}_2$  thickness, air hole diameter, refractive index, and wavelength, aiming to predict component confinement loss. For the first time, confinement loss values are processed for each wavelength and parameter, and systematically collected as sequential datasets for subsequent analysis. The dataset is then partitioned, with 80 percent allocated for training and 20 percent for testing in an ANN framework, the data processing flow from FEM to ML can be seen in Figure 8.

The developed ANN regression model utilizes the Sequential API from Keras, which is a high-level neural networks API that simplifies the construction and configuration of the model. The ReLU activation function has been selected for the input, output, and hidden layers due to its capability to introduce non-linearity, enabling the model to learn complex relationships within the data. The ReLU function is defined as follows:

$$f(x) = \max(0, x) \quad (8)$$

In this context,  $x$  represents the input to the neuron. The ReLU activation function has been shown to effectively mitigate the vanishing gradient problem, which occurs when the gradients of the loss function concerning the weights become very small, resulting in a slow or stagnant learning process. Additionally, ReLU accelerates convergence during training because it does not saturate and does not involve computationally expensive operations like exponentials [45]. A StandardScaler is applied to both the training and testing sets to standardize the features, which improves the model's performance and stability. The StandardScaler adjusts the input features to have a zero mean and unit variance, a common preprocessing step in machine learning. This process ensures that each feature contributes equally to the distance metric used by the model and prevents features with larger scales from dominating the optimization process [46].

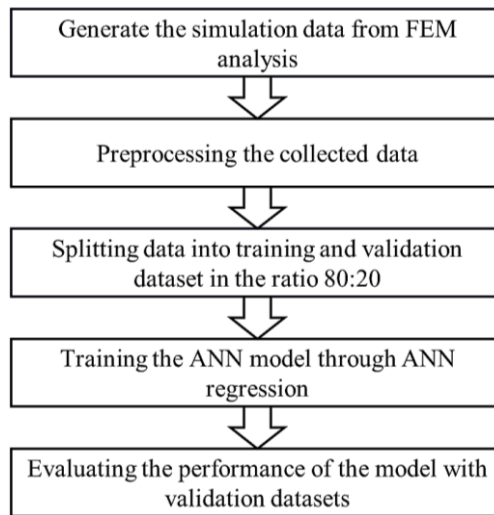


**Figure 8. Data processing flow from FEM to ML approaches**

The model is compiled using the Adam optimizer, which is an adaptive learning rate optimization algorithm that adjusts the learning rate for each parameter based on the first and second moments of the gradients. The Mean Squared Error (MSE) is used as the loss function, which measures the average squared difference between the actual and predicted values. The equation for MSE is defined as follows [47]:

$$MAE = \frac{\sum_{i=1}^n |y_i - \bar{y}_i|}{n} \quad (9)$$

where  $y_i$ ,  $\bar{y}_i$  and  $n$  represent the target, the mean of the target values, and the number of samples, respectively. The Mean Squared Error (MSE) serves as the loss function, measuring the average squared difference between the actual and predicted values. MSE is a popular choice for regression problems because it is both differentiable and convex, and it penalizes larger errors more significantly than smaller ones.

To train and test the ANN regression model, the collected datasets are divided into an 80:20 ratio. Validation sets are also utilized to evaluate the accuracy of actual outputs compared to predictions. Hyperparameters are systematically adjusted to minimize the Mean Squared Error (MSE), with model weights and biases updated iteratively. The hyperparameter optimization includes varying the number of nodes (10, 50, 100, 150, 200, 250) while using the Adam optimization algorithm. Simulation results indicate that the optimal MSE is achieved with 50 nodes (MSE: 0.00083), whereas the worst MSE occurs with 10 nodes (MSE: 0.7963). A noticeable trend in MSE is observed as the number of nodes changes, showing a decrease in MSE values as it reaches 200 nodes. Additionally, the effect of varying the number of hidden layers (from 1 to 5 layers) on MSE is explored, revealing that a configuration with a single hidden layer (MSE: 0.00087) performs best. The analysis also includes an examination of MSE trends over epochs, with the best performance noted at 5000 epochs (MSE: 0.00094). The findings are graphically represented in Figures 9-a and 9-b [22].

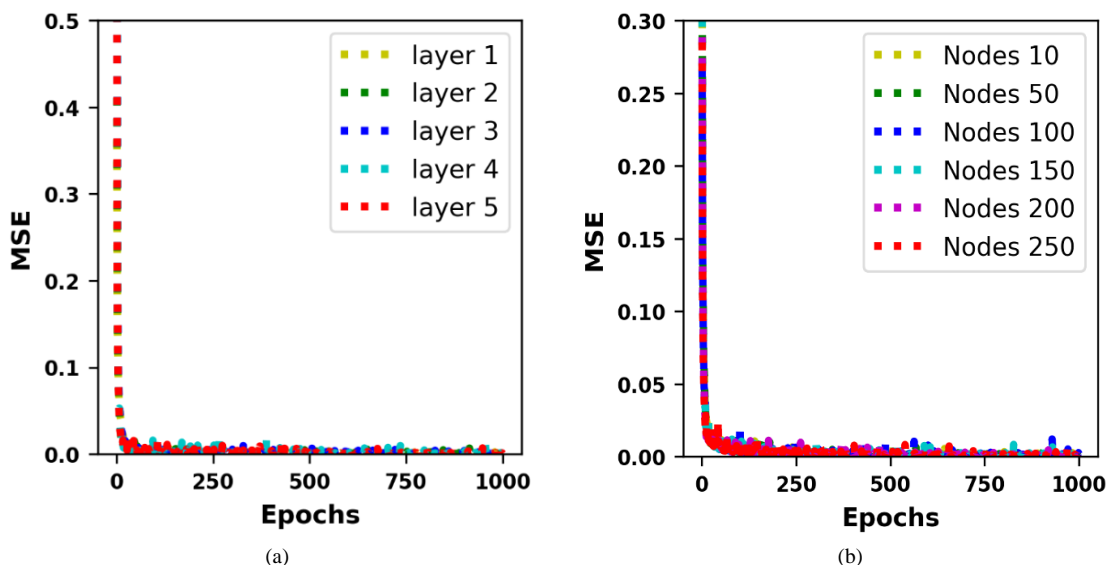


**Figure 9. epoch and MSE on sensor circuits, (a) layer variations from 1 to 5 layers, (b) node variations from 10 to 250 nodes**

### 3-7- Comparison Study

In comparison with previous studies, Kumar et al. (2023) [22] reported a photonic crystal fiber (PCF) component for detecting cancer cells, utilizing machine learning to optimize parameter variations and achieving a low Mean Squared Error (MSE) of 0.01525. The input parameters they used included gold thickness, air hole distance, and diameter, along with variations in the number of nodes from 10 to 40 and hidden layers from 1 to 3. Similarly, another study employed machine learning to analyze PCF for malaria detection, resulting in an MSE of 0.01526, with input parameters including gold thickness, air hole distance, diameter, wavelength, and sample refractive index. Verma et al. conducted related work with a training and validation data ratio of 90:10, achieving an MSE of 0.1163 (see Table 3). In our research, we focused on reducing the MSE while increasing the input parameters, which included gold thickness, TiO<sub>2</sub> thickness, air hole diameter, air hole distance, wavelength, and analyte refractive index. We varied the number of hidden layers from 1 to 5 and the number of nodes from 10 to 250. Our study reported a significantly lower MSE of 0.00083 in the implementation of machine learning on PCF-SPR sensor components.

**Table 3. Comparison with previous studies**

Sensitivity	Machine learning errors	Reference
13,071 nm/RIU (MCF-7 Cancer cells)	0.01525	Kumar et al. (2023) [22]
11,034 nm/RIU	0.1163	Verma et al. (2022) [48]
None	0.0007	Meng et al. (2023) [49]
12,142 nm/RIU	0.01526	Kumar et al. (2023) [31]
24,000 nm/RIU	0.00083	Present Studies

## 4- Conclusion

In this research, we report on an elliptical PCF-SPR sensor component integrated into one of the air holes in the core. This sensor can detect analytes within a refractive index range of 1.335 to 1.385 RIU. The sensor is constructed using fused silica as the dielectric material, with TiO<sub>2</sub> and gold as the plasmonic materials. Four polarization modes were identified in the component, exhibiting consistent resonance wavelength shifts. The maximum resonance wavelength (WS) shift in the refractive index range of 1.38 to 1.385 RIU was 24,000 nm/RIU, which is better than previously reported results. Additionally, amplitude sensitivity (AS) measurements were conducted on these sensor components, yielding maximum AS values of -91.82 1/RIU for x-polarized light, -91.88 1/RIU for y-polarized light, -90.98 1/RIU for x-odd, and -89.276 1/RIU for y-odd.

To optimize sensor performance, numerical data obtained from FEM analysis were used to create machine learning datasets. Predictions of resonance wavelength peaks were then performed, varying the number of nodes and hidden layers. Hyperparameter optimization involved adjusting the number of nodes (10, 50, 100, 150, 200, and 250) using the 'Adam' optimization algorithm. Simulation results indicated that the optimal Mean Squared Error (MSE) was achieved with 50 nodes (MSE: 0.00083), while the worst MSE was noted with 10 nodes (MSE: 0.7963). A noticeable trend in MSE was observed as the number of nodes varied, with MSE values decreasing upon reaching 200 nodes. The influence of varying the number of hidden layers (from 1 to 5) on MSE was also examined, revealing that the configuration with a single hidden layer (MSE: 0.00087) performed best. Furthermore, the analysis included an examination of MSE trends over epochs, identifying the best performance at 5000 epochs (MSE: 0.00094), which is significantly better compared to previous research.

## 5- Declarations

### 5-1- Author Contributions

Conceptualization, K.R., A.M., and A.M.N.F.S.; methodology, K.R., B.A., and M.Y.; software, K.R., H.C., and A.M.N.F.S.; validation K.R. and A.M.N.F.S.; formal analysis, K.R. and B.A.; investigation, A.M. and K.R.; resources, K.R.; data curation, B.A.; writing—original draft preparation, K.R., A.M.N.F.S., M.Y., and H.C.; writing—review and editing, K.R. and B.A.; visualization, A.M. and K.R.; supervision, K.R.; project administration, K.R.; funding acquisition, K.R. All authors have read and agreed to the published version of the manuscript

### 5-2- Data Availability Statement

The data presented in this study are available on request from the corresponding author.

### 5-3- Funding

LPDP Republic of Indonesia in the Domestic Masters scholarship scheme.

#### 5-4-Acknowledgements

We would like to thank LPDP of the Republic of Indonesia for providing funding for conducting research (KR, BA, MY, HC). Also, we thank the Bandung Institute of Technology for facilitating research.

#### 5-5-Institutional Review Board Statement

Not applicable.

#### 5-6-Informed Consent Statement

Not applicable.

#### 5-7-Conflicts of Interest

The authors declare that there is no conflict of interest regarding the publication of this manuscript. In addition, the ethical issues, including plagiarism, informed consent, misconduct, data fabrication and/or falsification, double publication and/or submission, and redundancies have been completely observed by the authors.

## 6- References

- [1] Amendola, V., Pilot, R., Frascioni, M., Maragò, O. M., & Iati, M. A. (2017). Surface plasmon resonance in gold nanoparticles: A review. *Journal of Physics Condensed Matter*, 29(20), 203002. doi:10.1088/1361-648X/aa60f3.
- [2] Nuzhat, S., Sultana, S., Hassan, M. F. Bin, Biswas, S. K., Das Gupta, M., & Talukder, H. (2021). Dual scaled approach SPR-based PCF RI sensor with ultra-low loss. *Journal of Physics: Conference Series*, 2070(1), 012109. doi:10.1088/1742-6596/2070/1/012109.
- [3] Sakib, M. N., Hossain, M. B., Al-tabatabaie, K. F., Mehedi, I. M., Hasan, M. T., Hossain, M. A., & Amiri, I. S. (2019). High performance dual core D-shape PCF-SPR sensor modeling employing gold coat. *Results in Physics*, 15. doi:10.1016/j.rinp.2019.102788.
- [4] Liu, W., Hu, C., Zhou, L., Yi, Z., Liu, C., Lv, J., Yang, L., & Chu, P. K. (2022). A square-lattice D-shaped photonic crystal fiber sensor based on SPR to detect analytes with large refractive indexes. *Physica E: Low-Dimensional Systems and Nanostructures*, 138. doi:10.1016/j.physe.2021.115106.
- [5] Ibrahim, K. M., Kumar, R., & Pakhira, W. (2023). Enhance the Design and Performance Analysis of a Highly Sensitive Twin-Core PCF SPR Biosensor with Gold Plating for the Early Detection of Cancer Cells. *Plasmonics*, 18(3), 995–1006. doi:10.1007/s11468-023-01825-w.
- [6] Guo, T., Zhang, T., Li, Y., & Qiao, X. (2020). Highly Sensitive FBG Seismometer with a 3D-Printed Hexagonal Configuration. *Journal of Lightwave Technology*, 38(16), 4588–4595. doi:10.1109/JLT.2020.2991667.
- [7] Irawan, D., Ramadhan, K., Saktioto, T., & Marwin, A. (2023). An optimum design of high sensitivity PMMA-coated FBG sensor for temperature measurement. *Telkomnika (Telecommunication Computing Electronics and Control)*, 21(2), 382–389. doi:10.12928/TELKOMNIKA.v21i2.22746.
- [8] Lee, B. (2003). Review of the present status of optical fiber sensors. *Optical Fiber Technology*, 9(2), 57–79. doi:10.1016/S1068-5200(02)00527-8.
- [9] Tosi, D., Macchi, E. G., Gallati, M., Braschi, G., Cigada, A., Rossi, S., Leen, G., & Lewis, E. (2014). Fiber-optic chirped FBG for distributed thermal monitoring of ex-vivo radiofrequency ablation of liver. *Biomedical Optics Express*, 5(6), 1799. doi:10.1364/boe.5.001799.
- [10] Yang, X., Yuan, Y., Dai, Z., Liu, F., & Huang, J. (2016). Optical property and adsorption isotherm models of glucose sensitive membrane based on prism SPR sensor. *Sensors and Actuators, B: Chemical*, 237, 150–158. doi:10.1016/j.snb.2016.06.090.
- [11] Horváth, R., Pedersen, H. C., Skivesen, N., Selmeczi, D., & Larsen, N. B. (2003). Optical waveguide sensor for on-line monitoring of bacteria. *Optics Letters*, 28(14), 1233. doi:10.1364/ol.28.001233.
- [12] Wu, T., Shao, Y., Wang, Y., Cao, S., Cao, W., Zhang, F., Liao, C., He, J., Huang, Y., Hou, M., & Wang, Y. (2017). Surface plasmon resonance biosensor based on gold-coated side-polished hexagonal structure photonic crystal fiber. *Optics Express*, 25(17), 20313. doi:10.1364/oe.25.020313.
- [13] Irawan, D., Ramadhan, K., Saktioto, Fitmawati, Hanto, D., Widiyatmoko, B., Marwin, A., & Azhar. (2023). Ultra-low loss and dual polarized SPR-PCF sensor based on refractive index. *Bulletin of Electrical Engineering and Informatics*, 12(6), 3325–3334. doi:10.11591/eei.v12i6.4293.
- [14] Sen, S., Hasan, M. M., & Ahmed, K. (2021). Ultra-Low Material Loss Quasi Pattern Based Photonic Crystal Fiber for Long Distance THz Wave Propagation. *Silicon*, 13(5), 1663–1673. doi:10.1007/s12633-020-00554-7.

- [15] Mahabubur Rahman, M., Aslam Molla, M., Kumar Paul, A., Based, M. A., Masud Rana, M., & Anower, M. S. (2020). Numerical investigation of a highly sensitive plasmonic refractive index sensor utilizing hexagonal lattice of photonic crystal fiber. *Results in Physics*, 18. doi:10.1016/j.rinp.2020.103313.
- [16] Falah, A. A. S., Wong, W. R., & Mahamd Adikan, F. R. (2022). Single-mode eccentric-core D-shaped photonic crystal fiber surface plasmon resonance sensor. *Optics and Laser Technology*, 145. doi:10.1016/j.optlastec.2021.107474.
- [17] Bing, P., Sui, J., Wu, G., Guo, X., Li, Z., Tan, L., & Yao, J. (2020). Analysis of Dual-Channel Simultaneous Detection of Photonic Crystal Fiber Sensors. *Plasmonics*, 15(4), 1071–1076. doi:10.1007/s11468-020-01131-9.
- [18] Yasli, A., Ademgil, H., Haxha, S., & Aggoun, A. (2020). Multi-Channel Photonic Crystal Fiber Based Surface Plasmon Resonance Sensor for Multi-Analyte Sensing. *IEEE Photonics Journal*, 12(1). doi:10.1109/JPHOT.2019.2961110.
- [19] Tahhan, S. R., & Taha, R. M. (2022). Mercedes Benz logo based plasmon resonance PCF sensor. *Sensing and Bio-Sensing Research*, 35. doi:10.1016/j.sbsr.2021.100468.
- [20] Ramola, A., Marwaha, A., & Singh, S. (2021). Design and investigation of a dedicated PCF SPR biosensor for CANCER exposure employing external sensing. *Applied Physics A: Materials Science and Processing*, 127(9), 643. doi:10.1007/s00339-021-04785-2.
- [21] Hoseinian, M. S., Ahmadi, A., Safaei Bezgabadi, A., & Bolorizadeh, M. A. (2021). Simulation of wagon wheel optical fiber biosensor for quick and easy detection of cancer cells. *Optical and Quantum Electronics*, 53(8), 427. doi:10.1007/s11082-021-02970-4.
- [22] Kumar, A., Verma, P., & Jindal, P. (2023). Surface plasmon resonance sensor based on MXene coated PCF for detecting the cancer cells with machine learning approach. *Microelectronic Engineering*, 267–268. doi:10.1016/j.mee.2022.111897.
- [23] Singh, S., & Prajapati, Y. K. (2023). Novel Bottom-Side Polished PCF-Based Plasmonic Biosensor for Early Detection of Hazardous Cancerous Cells. *IEEE Transactions on Nanobioscience*, 22(3), 647–654. doi:10.1109/TNB.2023.3233990.
- [24] Ehyae, A., Mohammadi, M., Seifouri, M., & Olyae, S. (2023). Design and numerical investigation of a dual-core photonic crystal fiber refractive index sensor for cancer cells detection. *European Physical Journal Plus*, 138(2), 129. doi:10.1140/epjp/s13360-023-03749-0.
- [25] Mittal, S., Saharia, A., Ismail, Y., Petruccione, F., Bourdine, A. V., Morozov, O. G., Demidov, V. V., Yin, J., Singh, G., & Tiwari, M. (2023). Spiral Shaped Photonic Crystal Fiber-Based Surface Plasmon Resonance Biosensor for Cancer Cell Detection. *Photonics*, 10(3), 230. doi:10.3390/photonics10030230.
- [26] Yan, X., Wang, Y., Cheng, T., & Li, S. (2021). Photonic crystal fiber SPR liquid sensor based on elliptical detective channel. *Micromachines*, 12(4), 408. doi:10.3390/mi12040408.
- [27] Otupiri, R., Akowuah, E. K., & Haxha, S. (2015). Multi-channel SPR biosensor based on PCF for multi-analyte sensing applications. *Optics Express*, 23(12), 15716. doi:10.1364/oe.23.015716.
- [28] Li, W., Chen, Y., Xu, J., Jiang, M., & Zou, H. (2023). A D-Shaped SPR-Based PCF Sensor with an Extremely High-Amplitude Sensitivity for Measuring the Refractive Index. *Micromachines*, 14(7), 1295. doi:10.3390/mi14071295.
- [29] Kalyoncu, C., Yasli, A., & Ademgil, H. (2022). Machine learning methods for estimating bent photonic crystal fiber based SPR sensor properties. *Heliyon*, 8(11), e11582. doi:10.1016/j.heliyon.2022.e11582.
- [30] Li, H., Chen, H., Li, Y., Chen, Q., Fan, X., Li, S., & Ma, M. (2023). Prediction of the optical properties in photonic crystal fiber using support vector machine based on radial basis functions. *Optik*, 275, 170603. doi:10.1016/j.ijleo.2023.170603.
- [31] Kumar, A., Verma, P., & Jindal, P. (2023). Machine learning approach to surface plasmon resonance sensor based on MXene coated PCF for malaria disease detection in RBCs. *Optik*, 274, 170549. doi:10.1016/j.ijleo.2023.170549.
- [32] Dogan, Y., Katirci, R., Erdogan, İ., & Yartasi, E. (2023). Artificial neural network based optimization for Ag grating D-shaped optical fiber surface plasmon resonance refractive index sensor. *Optics Communications*, 534, 129332. doi:10.1016/j.optcom.2023.129332.
- [33] Brixner, B. (1967). Refractive-Index Interpolation for Fused Silica\*. *Journal of the Optical Society of America*, 57(5), 674. doi:10.1364/josa.57.000674.
- [34] Sehmi, H. S., Langbein, W., & Muljarov, E. A. (2017). Optimizing the Drude-Lorentz model for material permittivity: Method, program, and examples for gold, silver, and copper. *Physical Review B*, 95(11), 115444. doi:10.1103/PhysRevB.95.115444.
- [35] Kumar, D., Khurana, M., Sharma, M., & Singh, V. (2023). Analogy of gold, silver, copper and aluminium based ultra-sensitive surface plasmon resonance photonic crystal fiber biosensors. *Materials Today: Proceedings*, 1-6. doi:10.1016/j.matpr.2023.02.319.
- [36] Divya, J., Selvendran, S., Raja, A. S., & Borra, V. (2024). A Novel Plasmonic Sensor Based on Dual-Channel D-Shaped Photonic Crystal Fiber for Enhanced Sensitivity in Simultaneous Detection of Different Analytes. *IEEE Transactions on Nanobioscience*, 23(1), 127–139. doi:10.1109/TNB.2023.3294330.

- [37] Majeed, M. F., & Ahmad, A. K. (2024). Design and analysis of a high sensitivity open microchannel PCF-based surface plasmon resonance refractometric sensor. *Optical Materials*, 147, 114617. doi:10.1016/j.optmat.2023.114617.
- [38] Singh, S., & Prajapati, Y. K. (2020). Dual-polarized ultrahigh sensitive gold/MoS<sub>2</sub>/graphene based D-shaped PCF refractive index sensor in visible to near-IR region. *Optical and Quantum Electronics*, 52(1), 17. doi:10.1007/s11082-019-2122-3.
- [39] Tian, M., Li, J., & Meng, F. (2023). Independent measurement of refractive index and temperature using D-gapped dual-channel structure in a photonic crystal fiber. *Optical and Quantum Electronics*, 55(4), 301. doi:10.1007/s11082-023-04616-z.
- [40] Ibrahim, K. M., Kumar, R., & Pakhira, W. (2023). A graphene/Au/TiO<sub>2</sub> coated dual-core PCF SPR biosensor with improved design and performance for early cancer cell detection of with high sensitivity. *Optik*, 288. doi:10.1016/j.ijleo.2023.171186.
- [41] Sarker, H., & Faisal, M. (2023). Surface plasmon resonance sensor using photonic crystal fiber for sucrose detection. *Sensing and Bio-Sensing Research*, 39. doi:10.1016/j.sbsr.2022.100544.
- [42] Sarker, H., Alam, F., Khan, M. R., Mollah, M. A., Hasan, M. L., & Rafi, A. B. M. S. (2022). Designing highly sensitive exposed core surface plasmon resonance biosensors. *Optical Materials Express*, 12(5), 1977. doi:10.1364/ome.452096.
- [43] Islam, M. R., Iftekher, A. N. M., Meraz, M. H. I., Nayen, M. J., & Khan, M. R. H. (2023). Design of a dual arrow shaped and dual plasmonic material compatible SPR PCF sensor. *Optical and Quantum Electronics*, 55(13), 1125. doi:10.1007/s11082-023-05364-w.
- [44] Piliarik, M., & Homola, J. (2009). Surface plasmon resonance (SPR) sensors: approaching their limits? *Optics Express*, 17(19), 16505. doi:10.1364/oe.17.016505.
- [45] Agarap, A. F. (2018). Deep Learning using Rectified Linear Units (ReLU). *arXiv Preprint*, arXiv:1803.08375. doi:10.48550/arXiv.1803.08375.
- [46] de Amorim, L. B. V., Cavalcanti, G. D. C., & Cruz, R. M. O. (2023). The choice of scaling technique matters for classification performance. *Applied Soft Computing*, 133. doi:10.1016/j.asoc.2022.109924.
- [47] Shams, S. R., Jahani, A., Kalantary, S., Moeinaddini, M., & Khorasani, N. (2021). The evaluation of artificial neural networks (ANN) and multiple linear regressions (MLR) models for predicting SO<sub>2</sub> concentration. *Urban Climate*, 37. doi:10.1016/j.uclim.2021.100837.
- [48] Verma, P., Kumar, A., & Jindal, P. (2022). Machine Learning Approach for SPR based Photonic Crystal Fiber Sensor for Breast Cancer Cells Detection. *2022 IEEE 7<sup>th</sup> Forum on Research and Technologies for Society and Industry Innovation (RTSI)*, 54, 7–12. doi:10.1109/rtsi55261.2022.9905187.
- [49] Meng, F., Ding, J., Zhao, Y., Liu, H., Su, W., Yang, L., Tao, G., Pryamikov, A., Wang, X., Mu, H., Niu, Y., He, J., Zhang, X., Lou, S., Sheng, X., & Liang, S. (2023). Artificial intelligence designer for optical Fibers: Inverse design of a Hollow-Core Anti-Resonant fiber based on a tandem neural network. *Results in Physics*, 46. doi:10.1016/j.rinp.2023.106310.